



A global evaluation of the JONSWAP spectra suitability on coastal areas

Ottavio Mattia Mazzaretto^{*,1}, Melisa Menéndez¹, Héctor Lobeto¹

IHCantabria - Instituto de Hidráulica Ambiental de la Universidad de Cantabria, Santander, Spain

ARTICLE INFO

Keywords:

Wave spectra
Wave climate
Hindcast
JONSWAP
Buoy
Peak-enhancement factor

ABSTRACT

Wave spectra provide comprehensive information on wave energy for different directions and frequencies. Integrated sea state parameters, however, are more commonly used for wave climate characterization. Many engineering applications estimate spectral conditions from these parameters using theoretical spectra. One of the theoretical spectra of widest practical use is the JONSWAP. Here, the wave spectra for the hindcasted 30 years covering coastal areas worldwide are studied. We first compare the simulated historical spectra against measurements from 39 buoys. Several approaches are raised in order to provide different information, such as a directional and frequency distribution and climate evaluation. The suitability of the JONSWAP spectrum is then analysed by exploring the best fit of the peak-enhancement factor from hourly sea states. Results show a peak-enhancement factor below 2.4, lower than the standard JONSWAP (i.e a value of 3.3), in most coastal areas and especially in the east coast of the continents, even for energetic hourly sea states. Tropical areas on the west coasts provide values close to the standard JONSWAP. Seasonal and inter-annual variations in the peak parameter are also investigated.

1. Introduction

A wide range of coastal engineering applications, such as harbour design and operability, route shipping, offshore structure design, and coastal erosion assessment needs a proper wave climate characterization. Most of these applications are based on integrated sea state bulk parameters (e.g. significant wave height (H_s), peak period (T_p) and Mean Wave Direction (MWD)). These parameters, however, do not provide a complete description of the complex and stochastic phenomenon of wind-generated ocean waves.

The directional wave spectrum (hereinafter $S(f, \theta)$) measures the variance of the distribution of the wave energy. Therefore, more information about the complexity of sea state is provided from the directional spectrum than the one provided by the bulk parameters.

The directional wave spectrum refers to the distribution of wave elevation variance as a function of both wave frequency (f) and wave direction (θ). This is defined in Eq. (1):

$$S(f, \theta) = \lim_{\Delta f \rightarrow 0} \lim_{\Delta \theta \rightarrow 0} \frac{1}{\Delta f \Delta \theta} \mathbb{E} \left[\frac{1}{2} a^2 \right] \quad (1)$$

where $\mathbb{E} \left[\frac{1}{2} a^2 \right]$ is the expected value of the variance ($\frac{1}{2} a^2$) and a is the amplitude (the underline indicates that the amplitude is treated as a random variable). Frequency spectrum ($S(f)$) and direction spectrum ($S(\theta)$) can be obtained with Eq. (2) and Eq. (3), respectively (Goda, 1988; Holthuijsen, 2007; Kamphuis, 2010).

Integrating the $S(f, \theta)$ in directions, from 0 to 2π , $S(f)$ is obtained:

$$S(f) = \int_0^{2\pi} S(f, \theta) d\theta \quad (2)$$

Integrating the $S(f, \theta)$ in frequencies (from f_{min} to f_{max}), $S(\theta)$ is obtained:

$$S(\theta) = \int_{f_{min}}^{f_{max}} S(f, \theta) df \quad (3)$$

The $S(f, \theta)$ is key information for wave modelling. For example, the wave spectrum is required to evaluate the interactions between waves and other matter such as forces on piles, breakwaters and offshore structures, the response of ships, platforms and floating breakwaters to waves, wave-induced erosion. The information contained in the $S(f, \theta)$ provides better wave model verification and data assimilation (Corbella et al., 2015).

Technological progress has made possible the development of new and more accurate measuring instrumentations. A good measure of the directional wave spectrum is still a great challenge despite its knowledge is more than 50 years old (Barstow et al., 2005).

In situ and remote sensing measurements are the two main sources of observation. The former includes submerged pressure sensors, buoys, acoustic or non-acoustic sensors for measuring wave orbital velocities, wave staffs and subsurface arrays of pressure sensors. The latter

* Corresponding author.

E-mail addresses: ottavio.mazzaretto@unican.es (O.M. Mazzaretto), melisa.menendez@unican.es (M. Menéndez), hector.lobeto@unican.es (H. Lobeto).

¹ Each author has worked equally to the paper.

includes marine radar (non-coherent and coherent), high frequency radar, lidar, satellites, optical sensors and altimeters (Iriah et al., 2000; Atkinson et al., 2005; O'Reilly et al., 1996; Steele et al., 1985).

For this study, in situ measurements of $S(f, \theta)$ are obtained from directional buoys. Maximum Entropy Method (MEM), Extended Maximum Entropy Method (EMEM), Direct Fourier Transform (DFT) and Maximum Likelihood Method (MLM) are some of the methods that could be used for the estimation of the directional wave spectrum (Kuik et al., 1988; Earle et al., 1999; Hashimoto and Konbune, 1988; Benoit, 1993; Brown et al., 2001; Lygre and Krogstad, 1986; Mitsuyasu et al., 1980; Goda, 1988; Longuet-Higgins, 1961).

Buoy measurements are used to validate the global directional wave spectrum hindcast. A reliable global directional wave spectrum hindcast could facilitate detailed characterization of the wave climate, especially in remote areas in which in situ measurements are not available. The existing global hindcasts are based on third wave generation spectral models such as WAM, SWAN or WW3, that explicitly parametrize all physical processes (degrees of freedom are the spectral bins) without imposing spectral shapes or energy levels (The WAVEWATCH III[®] Development Group, 2016). The approach to compare wave spectra depends on the available dimensions. For this study, directional wave spectra every 3 h over 30 years, each with 32 frequencies and 24 directional bins are available. Many studies, nonetheless, compare wave spectra focusing on the wave frequency spectrum (Garcia-Gabin, 2015; Mazaheri and Imani, 2019) or averaging the variability of hourly sea-states over larger time periods e.g. Echevarria et al. (2019). In this study, we assess four approaches to compare the directional wave spectrum from the hindcast ($S_H(f, \theta)$) against the directional wave spectrum from the buoys ($S_B(f, \theta)$), each of them focusing on different features.

In absence of wave spectra from hindcasts or in situ measurements, theoretical frequency spectra are available from literature, usually formulated in terms of H_s and T_p . Pierson–Moskowitz (PM), basis for the JONSWAP spectrum (both unimodal), the Ochi–Hubble and the Torsethaugen spectra (both multi-modal) are only some used examples (Hasselmann et al., 1973, 1980; Ochi and Hubble, 1977; Torsethaugen, 1993).

Nowadays, the JONSWAP spectrum has the highest practical usage in ocean related engineering studies. It has been used in multiple applications such as the evaluation of the performance of the recompilation methods of the $S(f, \theta)$ (e.g. MEM, MLM, DFT) under the effects of extreme sea states (Benoit, 1993). For the study of freak waves (Amuro and Ewans, 2019; Onorato et al., 2001), coastal downscaling (Camus et al., 2011), coastal structures design (Friesch et al., 2002), and loads on offshore floating structures (Magnusson et al., 2001; Takezawa and Kobayashi, 1989). Craciunescu and Christou (2020) offer an example of its usage, they conducted an experimental study on wave breaking dissipation in JONSWAP based waves. Another actual application is shown by Rossi et al. (2020), they compare different spectral estimation methods to evaluate the sea state parameters starting from a set of random sea state conditions characterized by random waves. It is also used to determine the wave crest distribution of nonlinear waves in shallow waters (Wang, 2014).

The JONSWAP spectrum is formulated as the PM spectrum multiplied by a peak-enhancement function which depends on the peak-enhancement factor and on the peak-width parameter (Eq. (12)). The peak-enhancement factor ranges from 1 to 7 (Goda, 1988) with a 3.3 mean value, widely applied in engineering works. Recent researches demonstrated the need for having a different value of γ . For example, Mazaheri and Imani (2019) showed for the Persian Gulf that different values of γ and σ_s can better reproduce storms, and Rueda-Bayona et al. (2020) showed a technique that uses a genetic algorithm to provide specific JONSWAP parameters.

The main goal of this study is to provide a global climate assessment of the performance of the JONSWAP spectrum. We have identified the

value of the peak-enhancement factor which best fits the hindcast frequency spectrum. For this purpose, 11643 grid points for 30 historical years of the GOW2 global wave hindcast database are analysed and the comparison of the hindcast against directional spectra information from buoys is first achieved. The study is organized as follows: the available data both hindcast and buoys, are presented in Section 2. Section 3 shows the comparison between the hindcast directional wave spectra against in situ measurements. Section 4 illustrates the methodology used for the assessment of the suitability of the JONSWAP spectrum. Finally, results are shown and discussed in Section 5. The comparison between the hindcast and the buoys is discussed, and the worldwide best fit of the JONSWAP spectrum is analysed from a climate and engineering point of view.

2. Data

2.1. Wave climate hindcast

The historical global wind wave hindcast used for this study is GOW2 (Perez et al., 2017). It is developed with third generation wave model WaveWatch III (WW3), which solves the spectral action density balance equation and is able to simulate global wave generation and propagation (Tolman, 2014). GOW2 hindcast extends from 1979 to the near present, providing hourly sea state parameters and 3-hourly frequency-direction wave spectra ($S_H(f, \theta)$) globally.

The numerical model was set up as follow: WW3 was implemented using the parametrization TEST451 (Ardhuin et al., 2010). Continuous ice treatment was applied to sea-ice concentrations with increasing levels of blocking for concentrations from 0.25 (no effect) to 0.75 (total blocking) (Tolman, 2003). SHOWEX movable-bed bottom friction based on field measurements from DUCK'94 and SHOWEX experiments was activated (Ardhuin et al., 2003; Hasselmann et al., 1973). The Discrete Interaction Approximation (DIA, (Hasselmann et al., 1985)) was used for the computation of the non-linear wave-wave interactions. Shallow water depth breaking following Battjes and Janssen (1978) with a Miche-style shallow water limiter for maximum energy was used. A third-order Ultimate Quickest propagation scheme (Leonard, 1979, 1991) with the correction for the garden sprinkler effect proposed by Tolman (2002) was activated. Hourly ice coverage and winds from the Climate Forecast System Reanalysis (CFSR from 1979 to 2010 (Saha et al., 2010) and with CFSv2 from 2011 to 2015 Saha et al. (2014)) were used. ETOPO1 bathymetry (Amante and Eakins, 2009) and coastlines proceedings from the Global Self-consistent, Hierarchical, High-resolution Geography Database (GSHHG, (Tomas et al., 2008)) were used.

The GOW2 wave hindcast is composed of four numerical domains in a multigrid two-way nesting approach (i.e. Global, Arctic, Antarctic and Coastal domain). Spatial resolution was increased from the global ($0.5^\circ \times 0.5^\circ$) to a quarter degree on the coastal domain. The coastal domain includes all the grid-points with depths below 200 m, all the oceanic islands and continental coasts within 1.5 degrees. Wave attenuation produced by islands and coastal features smaller than cell size was also considered by reducing the energy flux across discrete grid cell boundaries (Tolman, 2003). Reflection of shorelines was set to 0.05 and subgrid features were also considered. Note that due to the spatial resolution of the dataset (~ 25 km), localized surf processes which require higher spatial resolution are not considered. The wave spectra are defined by 24 direction bins and 32 frequencies ranging non-linearly from 0.0373 Hz to 0.7159 Hz with each frequency being 1.1 times the previous one. Directional sectors are 15° each. The hindcast has a total of 36455 grid-points with available spectra data. We select the nearshore and offshore locations of the coastal domain, obtaining ~ 8000 nearshore and ~ 3500 offshore ocean locations. We highlight that all the considered locations are offshore. The depth at the analysed points ranges from 5 to 4000 m. The JONSWAP climate

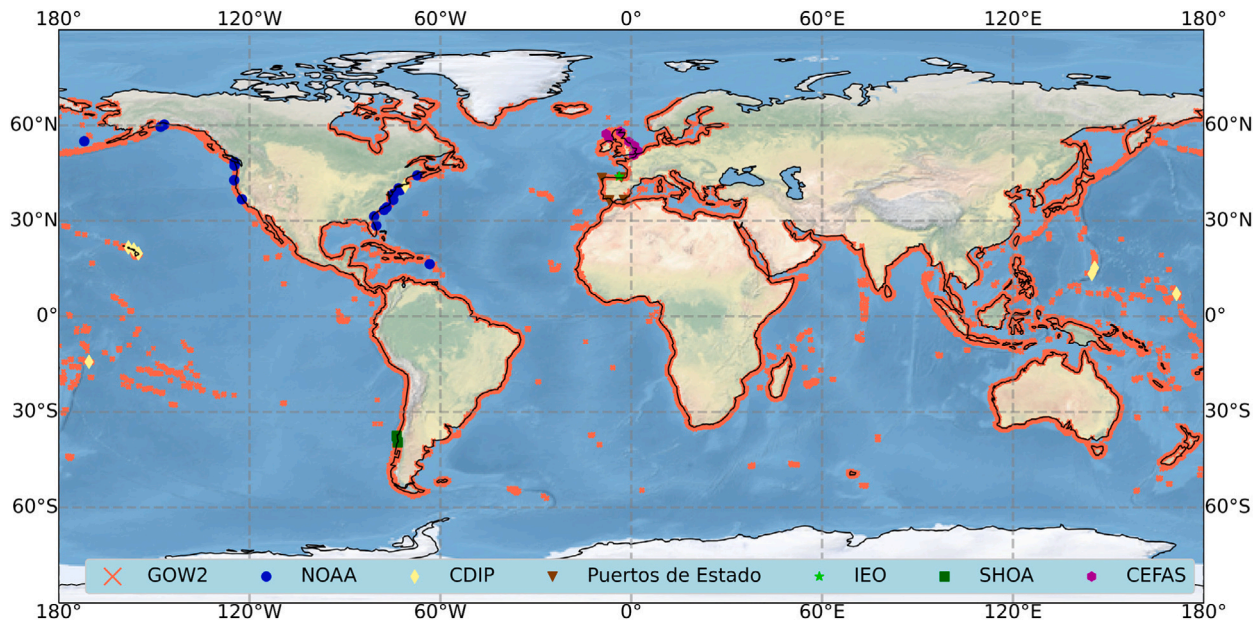


Fig. 1. Available $S(f, \theta)$ of the hindcast (GOW2) in red and of the six used databases (NOAA, CDIP, Puertos de Estado, IEO, SHOA and CEFAS).

analysis is carried out over 30 years (1989–2018) in the 11643 selected ocean locations (red crosses in Fig. 1).

Perez et al. (2017) show a global validation of H_s , mean period (T02) and MWD of the GOW2 hindcast against satellite altimeter data and 167 buoys worldwide. The database shows a good agreement against the observations, even through the areas affected by tropical cyclones.

2.2. Spectral data from buoys

Despite the huge number of available buoys worldwide, directional wave buoys are still limited. More than 80 directional wave buoys are identified, distributed across all ocean basins except for the Indian Ocean. All the data used in this study are freely available, except the data of SHOA (Chile), which can be requested through the website of the government. The institutions which provide the data are: NOAA (US coverage), CDIP (US and Pacific coverage), SHOA (Chilean coast), CEFAS (UK coverage), Puertos del Estado (PE) (ES coast) and IEO (only Santander, ES). Two conditions are set to the buoy records to be compared against hindcast data: (i) overlap with GOW2 of at least 12 complete months; (ii) in situ measurements must be within 0.25 [°] (~25 km) from the nearest GOW2 grid point.

The data provided by Chile do not fully meet the first criterion, but they are still considered in the analysis as they are the only available data in the extra tropical Southern Hemisphere. After this filtering, only the buoys illustrated in Fig. 1 are considered for the comparison. Building on these good previous validation results, we have extended the comparison against buoy measurements by comparing the hindcast directional spectra, $S_H(f, \theta)$, with the recorded spectra data from buoys, $S_B(f, \theta)$. Buoy coverage in North America and Europe is adequate, however spectral buoys in the Indian Ocean and in the South Atlantic are missing. Spectral buoys measure the 3D translation of a sea surface water particle within the time through equipped instrumentation such as accelerometers, GPS, tilt, pressure, angular rate or acoustic sensors. These measures are then processed to obtain the directional wave spectrum.

Information regarding ID, distance to the coast, coordinates, depth, number of available years, frequency range, Rawness Level (RL) and the estimating method are available in Table 1. The RL represents the grade of the post-processing available from buoy data. We classify RL in five categories (from 0 to 4, the lower the level the rawer the information):

Level 0: no post-processing. The data provided are directly the raw outputs of the buoy, such as the acceleration of the x, y, z axes.

Level 1: basic post-processing. The data provided are the BIG 3 (Heave, Pitch and Roll).

Level 2: medium post-processing. The data provided are the First Five (the frequency spectrum, $S(f)$, and the four lowest Fourier coefficients of the directional distribution of the wave energy (a_1, a_2, b_1, b_2)).

Level 2.1: medium-high post-processing. First Five provided in polar coordinates ($r_1, r_2, \theta_1, \theta_2$) which depend on a_1, a_2, b_1, b_2 .

Level 3: high post-processing. The Disp-Dir (MWD(f) and disprMWD(f)) is provided. The MWD(f) is the mean wave direction that depends on the frequency and the disprMWD(f) is the directional dispersion associated with the MWD, which also depends on the frequency.

Level 4: full post-processing. $S(f, \theta)$ is provided.

Each database requires a different method to estimate the $S(f, \theta)$. Concerning the NOAA database, the reference manual is used (Brown et al., 2001). The CDIP provides all the levels, except for the 2.1. Thus, we use the already compiled directional wave spectrum. Chile also provides the already compiled $S(f, \theta)$, whereas the WAFO² toolbox with MEM method starting from the BIG 3 is used for Puertos del Estado. Concerning the buoys of AGL and CEFAS, we consider the Disp-Dir data, hence the method proposed by Mitsuyasu et al. (1980) is implemented.

3. Comparison between the hindcast and the buoy directional wave spectra

Directional wave spectra from buoys differ from each other in frequency, direction and time resolution. We scale the $S_B(f, \theta)$ to 3-hourly timing and also the frequency and directional bins to be homogeneous with the $S_H(f, \theta)$. In addition, a preprocessing of the $S_B(f, \theta)$ is required in order to properly compare both databases. First a quality control in the spectral data of the buoy is conducted. The institutions provide the $S_B(f, \theta)$ and the already computed bulk parameters (e.g H_{s_i} and T_{p_i}). Time comparison between H_{s_i} and T_{p_i} against H_{s_B} and T_{p_B} (computed from $S_B(f, \theta)$) is performed. Outliers

² <http://www.maths.lth.se/matstat/wafo/>

Table 1

Selected directional wave buoys. First column is the ID of the buoy. Second column is the distance from the shore in [Km]. Third and fourth columns are the latitude and the longitude; the 5th is the water depth [m]. The 6th column represents the available years; the 7th is the frequency range; the 8th column is Rawness Level (RL) of available processed spectrum data and the last column (9th) is the used method of compilation.

ID	Dist.[Km]	LAT [°]	LON [°]	Depth [m]	NYears	f [Hz]	RL	Method			
CDIP 106	6.2	21.67048	-158.117	200	19 [2001–2019]						
CDIP 121	1.5	13.35417	144.7883	200	16 [2003–2018]	0.025–0.58	0–4 [no 2.1]	O'Reilly et al. (1996)			
CDIP 154	55	40.96887	-71.1268	50	10 [2009–2018]						
CDIP 163	1.3	7.0835	171.3918	553	9 [2011–2019]						
CDIP 189	7	-14.2732	-170.501	55	6 [2014–2019]						
CDIP 188	7.3	19.779	-154.97	345	7 [2012–2018]						
CDIP 187	11.7	21.01857	-156.422	200	6 [2014–2019]						
CDIP 197	9	15.26803	145.6623	488	4 [2015–2018]						
CEFAS 6201058	45	51.9525	2.1087	41	4 [2016–2019]	0.05–0.26	3	Mitsuyasu et al. (1980)			
CEFAS 62046	28	57.9667	-3.3333	54	12 [2008–2019]						
CEFAS 62047	45	56.12028	-7.06139	97	11 [2009–2019]						
CEFAS 62048	30	57.29217	-7.9142	100	11 [2009–2019]						
CEFAS 62288	16	50.7462	0.754	43	17 [2003–2019]						
CEFAS 62289	58.5	53.5307	1.055	22	17 [2003–2019]						
CEFAS 62293	39	54.919	-0.7487	66	14 [2006–2019]						
Chile Corral	8	-39.55	-73.41	150	2 [2012–2013]	0–0.64	4	-			
Chile Lebu	11.6	-37.59	-73.76	150	2 [2011–2012]						
NOAA 41008	36	31.4	-80.868	14.9	10 [2006–2018]	0.033–0.47	2.1	MEM (Brown et al., 2001)			
NOAA 41009	34	28.508	-80.185	42	7 [2012–2018]						
NOAA 41013	50	33.436	-77.743	23.5	16 [2003–2018]						
NOAA 41036	52	34.207	-76.949	-	10 [2006–2015]						
NOAA 42060	114	16.413	-63.354	1507	6 [2013–2018]						
NOAA 44009	30	38.457	-74.702	30	8 [1997–2018]						
NOAA 44014	92	36.606	-74.84	47	19 [1998–2018]						
NOAA 44025	43	40.251	-73.164	36.3	21 [1997–2018]						
NOAA 44027	28.4	44.283	-67.3	185.3	4 [2015–2018]						
NOAA 44066	140	39.618	-72.644	78	6 [2013–2018]						
NOAA 46015	24	42.771	-124.843	400	11 [2008–2018]						
NOAA 46041	31.5	47.353	-124.742	128	16 [1998–2018]						
NOAA 46042	46	36.785	-122.398	1645.9	20 [1998–2018]						
NOAA 46061	6.8	60.238	-146.833	222	5 [2014–2018]						
NOAA 46073	270	55.031	-172.001	3051.5	5 [2014–2018]						
NOAA 46076	31	59.502	-147.99	195.1	4 [2015–2018]						
NOAA 46087	10.46	48.493	-124.726	260.6	14 [2004–2018]						
PE Bilbao	32	43.64	-3.09	870	5 [2005–2009]				0–0.5	1,3	MEM (WAFO Group, 2011)
PE Cadiz	54.5	36.48	-6.96	450	6 [2003–2008]						
PE Gata	20.3	36.57	-2.32	536	5 [2004–2008]						
PE Villano	32	43.5	-9.21	385	9 [1998–2007]						
AGL IEO	48	43.906	-3.808	2850	7 [2009–2015]	0.06–0.51	1,3	Mitsuyasu et al. (1980)			

are identified if the value of H_{s_B} and T_{p_B} are more than 30% higher or lower than the H_{s_i} and T_{p_i} . The $S_H(f, \theta)$ within a radius of $0.25[^\circ]$ (around 25 Km) are then spatially interpolated to the same coordinates of the buoys. The spatial interpolation is carried out using the inverse distance weighting (Lu and Wong, 2008), choosing the hyper parameter (p) as 1 and d as the Euclidean distance.

Hourly sea states, with energy (averaged in directions and frequencies) lower than $0.001 [m^2/(Hz \text{ rad})]$ are not considered. Once the $S_B(f, \theta)$ has the same resolution in time, frequency and directions, the comparison with the hindcast is possible. The approaches and the metrics to compare both datasets are shown in Fig. 2. The matrices depicted in Fig. 2 are the $S(f, \theta)$, while the vectors are the $S(f)$ and the $S(\theta)$. The metrics in normal font are scalars, overlined are vectors and matrices in **bold**. Four different approaches to compare the directional wave spectrum from the hindcast against in situ data are proposed taking into account its complexity.

Fig. 2 first panel, shows the *global approaches* (hereinafter GA_g and GA_i). It is computed comparing the time averaged spectra ($\overline{S(f)}$, $\overline{S(\theta)}$ and $\overline{S(f, \theta)}$) of the hindcast against the one of the buoy. The second panel illustrates the *matrix approach* (hereinafter MA) which compares the frequency-direction bins of the spectra at each time step. The third panel depicts the *polar approach* (hereinafter PA), which is computed comparing every frequency-direction bin through time. The fourth approach (*1D Spectrum* (hereinafter *IDS*)) compares the 1D frequency spectrum ($S(f)$, Eq. (2)) through frequencies and the direction spectrum ($S(\theta)$, Eq. (3)) through directions at each time step.

Each approach is useful to understand a different characteristics of the directional wave spectrum. *GA*, *MA* and *IDS* are more practical for engineering applications, providing a quick and understandable view of the hindcast performance for time varying sea states. The performance of the $S(f, \theta)$, $S(f)$ or $S(\theta)$ with multiple sea and swells, however, might be hardly understandable. *PA* thus overcomes this issue. This approach provides wave climate information and makes more easily comprehensible not only in which frequencies and directions bin the energy is over or underestimated by the hindcast, but also if the climate pattern is followed during the time record. Fig. 2 also illustrates the metrics computed for each approach. A total of eight different metrics are analysed. The metrics are a function of the number of compared data (N), which depend on the dimension considered for the comparison. Concerning GA_g , *IDS* and *PA* the metrics shown from Eq. (4) to Eq. (7) are evaluated. In these equations \overline{B} and \overline{H} appear. These can represent different variables. For GA_g and *IDS* they are $S_B(f)$ and $S_H(f)$ or $S_B(\theta)$ and $S_H(\theta)$. The number of data are $N = \text{length of frequency (32)}$ or $N = \text{length of directions (24)}$, respectively. Concerning the *PA* they are the frequency-direction bins through time. Therefore the number of considered data are $N = \text{length of time}$.

1. SI: Scatter Index:

$$SI = \frac{\sqrt{\frac{1}{N} \sum_{i=1}^N (B_i - H_i)^2}}{\sqrt{\frac{1}{N} \sum_{i=1}^N B_i^2}} \quad (4)$$

The metric ranges from 0, indicating identical data, to ∞ .

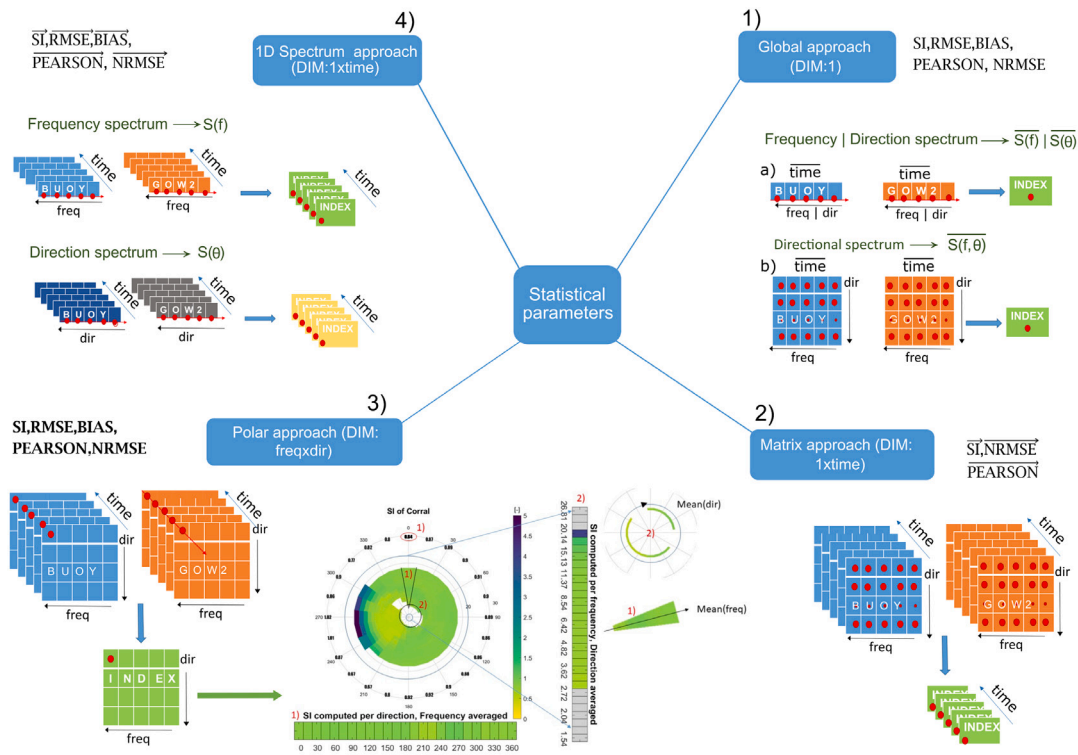


Fig. 2. Summary of the used approaches and metrics for the comparison of the $S_H(f, \theta)$ against $S_B(f, \theta)$.

2. RMSE: Root Mean Square Error:

$$RMSE = \sqrt{\frac{1}{N} \sum_{i=1}^N (B_i - H_i)^2} \quad (5)$$

RMSE ranges from 0 to ∞ .

3. BIAS:

$$BIAS = \frac{1}{N} \sum_{i=1}^N (B_i - H_i) \quad (6)$$

BIAS ranges from $-\infty$ to ∞ .

4. Pearson: Correlation Coefficient (Ccoef):

$$Ccoef = \frac{1}{N-1} \sum_{j=1}^N \left(\frac{H_j - \bar{H}}{\sigma_H} \right) \left(\frac{B_j - \bar{B}}{\sigma_B} \right) \quad (7)$$

Ccoef does not describe the error between the buoy and the hindcast, but describes the correlation between the two. The correlation coefficient ranges from -1 to 1 . A value of 1 implies a perfect concordance between the buoy and the hindcast.

Eq. (8) to Eq. (10) are used to compute the metrics for GA_b and MA . These metrics, also depend on the number of considered data, more precisely frequencies and directions are simultaneously compared: N = length of directions (24) and M = length of frequencies (32).

5. NRMSE Matrix: Normalized Root Mean Square Error of a Matrix (Echevarria et al., 2019), calculated at 3 h time resolution:

$$NRMSE_{matrix} = \sqrt{\frac{1}{MN} \sum_{i=1}^M \sum_{j=1}^N (S_B(i, j) - S_H(i, j))^2} * 100 / \max(S_H(f, \theta)) \quad (8)$$

NRMSE metric ranges from 0 to ∞ .

6. SI Matrix: Scatter Index expanded to the frequency-directional spectrum. This index was proposed for the $S(f)$ by Garcia-Gabin (2015).

$$SI_{matrix} = \frac{\sqrt{\frac{1}{MN} \sum_{i=1}^M \sum_{j=1}^N (S_B(f_i, \theta_j) - S_H(f_i, \theta_j))^2}}{\sqrt{\frac{1}{MN} \sum_{i=1}^M \sum_{j=1}^N (S_B(f_i, \theta_j))^2}} \quad (9)$$

This metric ranges from 0, indicating identical spectra, to ∞ .

7. Pearson Matrix:

$$Ccoef_{matrix} = \frac{\sum_{i=1}^M \sum_{j=1}^N (S_H(f_i, \theta_j) - \overline{S_H(f, \theta)})(S_B(f_i, \theta_j) - \overline{S_B(f, \theta)})}{\sqrt{\sum_{i=1}^M \sum_{j=1}^N (S_H(f_i, \theta_j) - \overline{S_H(f, \theta)})^2} \sqrt{\sum_{i=1}^M \sum_{j=1}^N (S_B(f_i, \theta_j) - \overline{S_B(f, \theta)})^2}} \quad (10)$$

Ccoef matrix value has the same meaning of the Pearson coefficient of Eq. (7). $S(f, \theta)$ represents the directional wave spectrum averaged in frequencies and directions.

4. JONSWAP fitting

A mathematical relation for the high frequencies tail of the spectrum (when $f > f_p$) was proposed by Phillips (1958). This relation is based on an “equilibrium range” in the wave spectrum, since the wave breaking is highly dominated by the gravity acceleration (g) and frequency (f). The proposed relation follows:

$$\Phi(\omega) \sim \alpha g^2 \omega^{-5} \quad (11)$$

where α is the Phillips constant, ω is the angular frequency in [rad/s] which can be replaced by the frequency ($f = \frac{\omega}{2\pi}$).

Many studies since Phillips (1958) confirmed the shape of the tail is modelled by f^{-5} (e.g Pierson (1976), Hasselmann et al. (1973), Holthuijsen (2007)).

Literature offers plenty of theoretical wave spectra. The JONSWAP (JOint North SeaWAVE Project, Hasselmann et al. (1973)) spectrum is

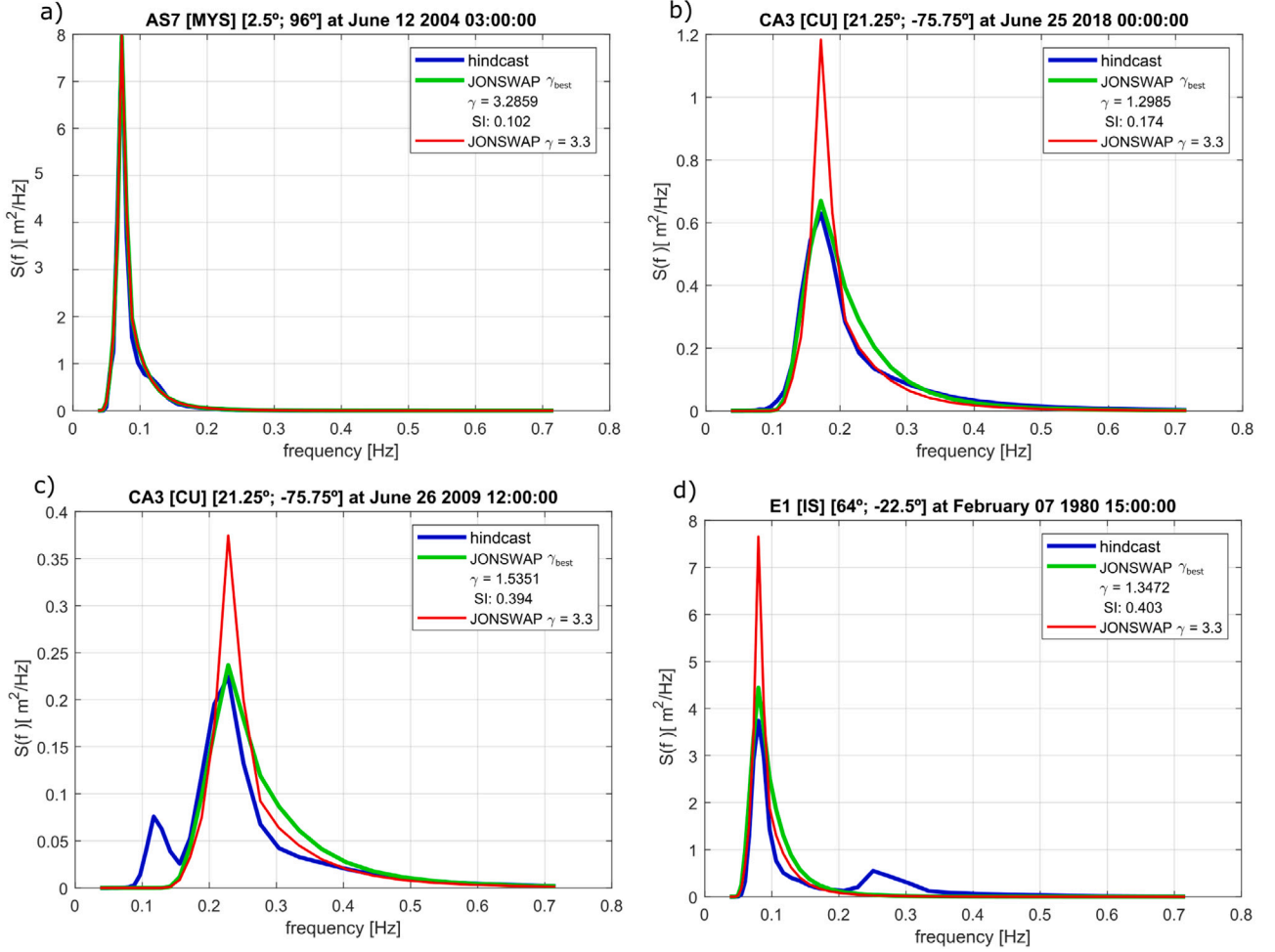


Fig. 3. Frequency spectra from 3 h sea state of the hindcast (blue), the best fit γ JONSWAP (green) and standard JONSWAP ($\gamma = 3.3$, red).

one of the most used in engineering studies. The JONSWAP spectrum is the result of a multinational project to characterize theoretical wave spectra function based on experiments conducted in the Southeast part of the North Sea. Although the JONSWAP spectrum is valid for not fully developed sea states, it is often used under fully developed sea states (Holthuijsen, 2007). The general expression of the idealized JONSWAP is (Hasselmann et al., 1973):

$$S_{JONSWAP}(f) = \alpha g^2 (2\pi)^{-4} f^{-5} \exp \left[-\frac{5}{4} \left(\frac{f}{f_p} \right)^{-4} \right] \gamma \exp \left[-\frac{1}{2} \left(\frac{f/f_p - 1}{\sigma} \right)^2 \right]$$

where,

$$\sigma = \begin{cases} \sigma_a, f \leq f_p \\ \sigma_b, f > f_p \end{cases} \quad (12)$$

The original equation contains five parameters, f_p , α , γ , σ_a and σ_b . f_p represents the peak frequency (at the maximum of the spectrum), α is the Phillips constants, the remaining three parameters γ , σ_a and σ_b define the shape of the spectrum. The σ_a and σ_b define the left and right sided widths of the spectral peak, respectively. The peak-enhancement factor (γ) characterizes the JONSWAP spectrum, $S_J(f)$, controlling the sharpness of the spectral peak. Goda (1988) proposed a formulation which depends only on the H_s and T_p , which is widely applied in the marine engineering community:

$$S_J(f) = \beta_J H_s^2 T_p^{-4} f^{-5} \exp[-1.25(T_p \cdot f)^{-4}] \cdot \gamma \exp[-(T_p \cdot f - 1)^2 / 2\sigma^2] \quad (13)$$

in which

$$\beta_J = \frac{0.0624}{0.230 + 0.0336\gamma - 0.185(1.9 + \gamma)^{-1}} [1.094 - 0.01915 \ln(\gamma)],$$

$$\sigma = \begin{cases} \sigma_a = 0.07, f \leq f_p \\ \sigma_b = 0.09, f > f_p \end{cases} \quad (14)$$

$$\gamma \in [1, 7]$$

Although Goda (1988) showed that in different regions of the world the peak-enhancement factor should vary, it is in general considered with its mean value ($\gamma = 3.3$). The value of γ that best fits the $S_J(f)$ for each sea-state of $S_H(f)$ can be estimated minimizing the SI between the two spectra (Eq. (15)), in which the number of data considered (N) is the frequencies (32). We refer to the estimated peak-enhancement factor as γ_{best} . We estimate the performance of the fitting using the scatter index as follows:

$$SI = \frac{\sqrt{\frac{1}{N} \cdot \sum_{i=1}^N (S_H(f_i) - S_J(f_i))^2}}{\sqrt{\frac{1}{N} \cdot \sum_{i=1}^N S_H(f_i)^2}} \quad (15)$$

SI compares the $S_J(f)$ with the $S_H(f)$ along the frequencies.

Fig. 3 illustrates four examples of the JONSWAP spectrum using γ_{best} (green line, hereinafter best JONSWAP), the usual $\gamma = 3.3$ (red line, hereinafter standard JONSWAP) and the frequency spectrum from the hindcast (blue line). These examples are intended to show the most common real case studies that appear in wave climate. Overall, we found that the best JONSWAP spectrum has similar peak energy

and area to the one of the hindcast, whereas the standard JONSWAP overestimates the peak energy. The fitting and its performance are computed at each time step (3-hourly sea state over 30 years, from 1989 to 2018) for each of the 11643 studied locations. From this study we can also analyse when the spectral shape of S_H and S_J differs even if the bulk sea state parameters are similar. Fig. 3 (panel (a), AS7, Asia, Malaysia [2.5°, 96°]) shows a good shape agreement between the best JONSWAP and the hindcast frequency spectrum with $\gamma_{best} \sim 3.3$. Panel (b) (CA3, Central America, Cuba [21.25°, -75.75°]) however, shows that the standard JONSWAP overestimates the energy peak and the best JONSWAP, with $\gamma \sim 1.3$ models better the shape of the hindcast. Panels (c) and (d) of Fig. 3 illustrate the problem of the multi-peaked spectra. Only the peak with highest energy is well represented by the best JONSWAP (AFR10, Africa, Madagascar [20.75°, 72.75°] and E1, Europe, Island [64°, -22.5°]), thus a multimodal theoretical wave spectrum would be preferred.

The spectral shape is a basis parameter concerning ocean related engineering studies. Nonetheless, differences in shape cannot be appreciated comparing only H_s . Indeed, the H_s between the standard JONSWAP, the best JONSWAP and the hindcast spectrum is similar despite their shapes being different.

The evaluation of the JONSWAP performance is carried out with the SI (Eq. (15)). This metric can vary from 0 (no error) to ∞ (high error). In order to facilitate the understanding of the global results, five qualitative SI ranges are defined based on the analysis of the differences in the area, energy peak, H_s , T_e , Pearson coefficient and kurtosis for different values of the SI for 60 locations. The area represents the differences between the area under the curves. The energy peak is the difference between the magnitude of the maximum energy. ΔH_s is the difference in significant wave height. ΔT_e is the difference in the energetic period. Pearson coefficient represents the capacity of the best JONSWAP to follow the pattern of the hindcast spectrum and, the kurtosis represents the sharpness or the broadness of the spectrum. We set the upper limit of the SI to 1, as $SI > 1$ provides more than 40% of error in all the metrics except for the ΔH_s , which does not depend on the shape of the spectrum, then having high values of SI does not undermine the H_s . SI ranging between 0–0.2 results in errors lower than the 15%, 0.2–0.4 errors between 15%–20%, 0.4–0.6 errors between 20%–30% and between 0.6–0.8 30%–40%. Therefore, the final ranges are: $0 \leq SI \leq 0.2$ Very good, $0.2 < SI \leq 0.4$ Good, $0.4 < SI \leq 0.6$ not good, $0.6 < SI \leq 0.8$ Poor and $0.8 < SI \leq 1$ Very poor.

Note that the qualitative ranges developed here are specifically for the comparison between the hindcast and the fitted JONSWAP spectra. These ranges are intended as a guide to understand the fitting of the JONSWAP spectra. Therefore, similar ranges do not apply to the comparison between the buoy data and the hindcast

5. Results & discussion

5.1. Comparison of the hindcast spectra with buoy observations

Before assessing the suitability of the JONSWAP spectrum from the GOW2 hindcast, we compare the hindcast spectra data against measured spectra from buoys to evaluate the reliability of $S(f, \theta)$. The comparison is done according to the approaches described in Section 3 (Fig. 2).

Fig. 4 depicts a comparison of the spectral data at two of the analysed buoys: AGL IEO [43.906°; -3.808°], Santander (ES) in the European Atlantic Ocean and CDIP 154 [40.96887°; -71.1268°] Rhode Island (US) in the US Atlantic Ocean. Top panels, (a) and (c), represent the averaged directional wave spectrum. On the right (left) there is the GOW2 hindcast (buoy). Lower panels, (b) and (d), represent the averaged frequency spectrum (left) and the averaged direction spectrum (right). Concerning AGL IEO buoy (panels (a) and (b)) the main direction where the energy comes from is 270–330[°] for both the hindcast and the buoy. The buoy shows a higher directional dispersion

than the hindcast for energy coming from 180–270[°]. The hindcast does not include this energy, nor the one from 0–30[°]. Similar behaviour can be seen in panel (b) (right), where the direction spectrum is illustrated. The hindcast overestimates the energy from 300[°] and underestimates the one coming from 0–30[°] as the one coming from 180–270[°]. In contrast, the frequency spectrum (panel (b), left) shows a good agreement with a minor underestimation of the energy. CDIP 154 is shown in Fig. 4, panels (c) and (d). This location shows three energy peaks at 135, 180 and 195[°]. The hindcast does not entirely follow this behaviour, showing peaks of energy at 180 and 195[°], but not the one at 135[°]. In contrast to AGL IEO, the directional spread of the buoy is well described. Concerning the frequency spectrum, panel (d), it can be seen a good agreement between the hindcast and the buoy. The direction spectrum also shows a good agreement even if the peaks of energy are not represented, the energy distribution and magnitude is similar and the directional spread is well represented.

Showing the mean wave climate conditions of these locations leads to a better understanding of the performance of the hindcast through the approaches shown in Fig. 2.

Fig. 5, panel (a), illustrates the *IDS* for the $S(f)$ of the buoy of CDIP 154. Left axis (blue) illustrates the hourly RMSE values, right axis (red) represents the monthly-averaged hourly RMSE. The RMSE for both, $S(f)$ and $S(\theta)$ (not shown), is low for the whole time record with some peaks for specific hourly sea states. The monthly average of the RMSE stays under 1 [m² s] and 0.1 [m²/rad] for the frequency and direction spectra, respectively. Fig. 5(b) shows the time-averaged RMSE of the $S(f)$ for each buoy. RMSE does not exceed more than 1.5 [m² s] for most of the locations. The highest values are found for the buoys located in Chile, Northern Ireland and Spain.

Fig. 6 shows a monthly comparison using the *MA* between the hindcast and six of the selected buoys, one per database. For these locations, the monthly $S(f, \theta)$ of the hindcast performs well, the nRMSE stays always under 9% and the Pearson coefficient stays above 0.8 (except for CDIP 154 in September). In general, there are no significant variations of the nRMSE and the Pearson coefficient within the year. The most fluctuating locations seem to be CDIP 154 and Villano. Villano has a peak of nRMSE and a local minimum of the Pearson coefficient in October. Regarding CDIP 154, the nRMSE fluctuates during the whole year, it starts at around 6% and fluctuates until October, where it stabilizes around 6% again. The lowest and the highest values are reached in July (3%) and in September (9%), respectively. The Pearson coefficient fluctuates a little until September, where it falls from 0.9 to 0.6. After this month, it rockets again to a value above 0.9. The rest of the buoy locations present a more stable pattern within a year.

The last shown approach is the *polar approach* (Fig. 7). Concerning the BIAS of CDIP 154 (Fig. 7, upper panels), the hindcast can achieve the same directional dispersion as the buoy. The energy in the peak direction is underestimated and the energy in the secondary directions is overestimated. The buoy has more energy than the hindcast for lower periods, while the hindcast overestimates the energy for higher periods. The Pearson coefficient and the SID show that the higher the energy the higher the agreement. The SID and the Pearson coefficient, regarding the Santander IEO buoy (Fig. 7, lower panels), show, as for the CDIP 154, higher accordance where the energy is higher. The BIAS shows that the hindcast overestimates the energy coming from the peak direction (315–345°) whereas underestimates the energy for the secondary directions, due to the lower directional spread.

The approaches and the metrics illustrated in Fig. 2 are computed for each buoy. Table 2 summarizes three approaches for the comparison of the hindcast against 39 buoys. The first column shows the GA_b , the second column the *MA* (time-averaged), in the last column is depicted the *IDS* for $S(f)$ spectrum (time-averaged). Table 2 summarizes the data of *IDS* $S(f)$, *MA* and GA_b approaches. Regarding the GA_b , nRMSE is small for most of the buoys, it remains lower than 15%. The highest values are found in Bilbao, Gata, NOAA 46080 and Lebu. The SI metric also shows good agreement. Concerning the *MA*, the nRMSE remains

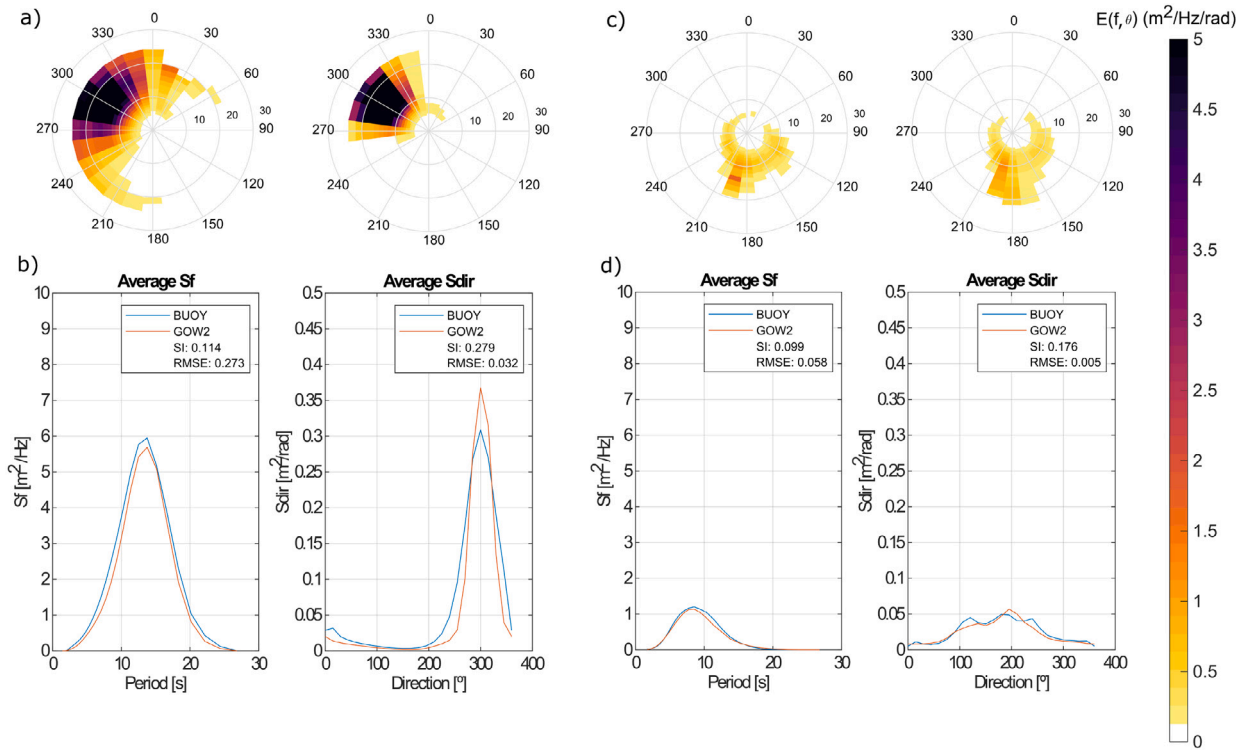


Fig. 4. Panel (a)–(b): AGL IEO ([143.906°; −3.808°], Santander (ES)) and Panel (c)–(d): CDIP 154 ([140.96887 °; −71.1268°], Rhode Island (US)). Top panels represent the time averaged $S(f, \theta)$, on the left (right) is depicted the buoy (hindcast). Bottom panel represents the time averaged frequency spectrum, on the left, and on the right the direction spectrum, blue line is the buoy, orange line is the GOW2.

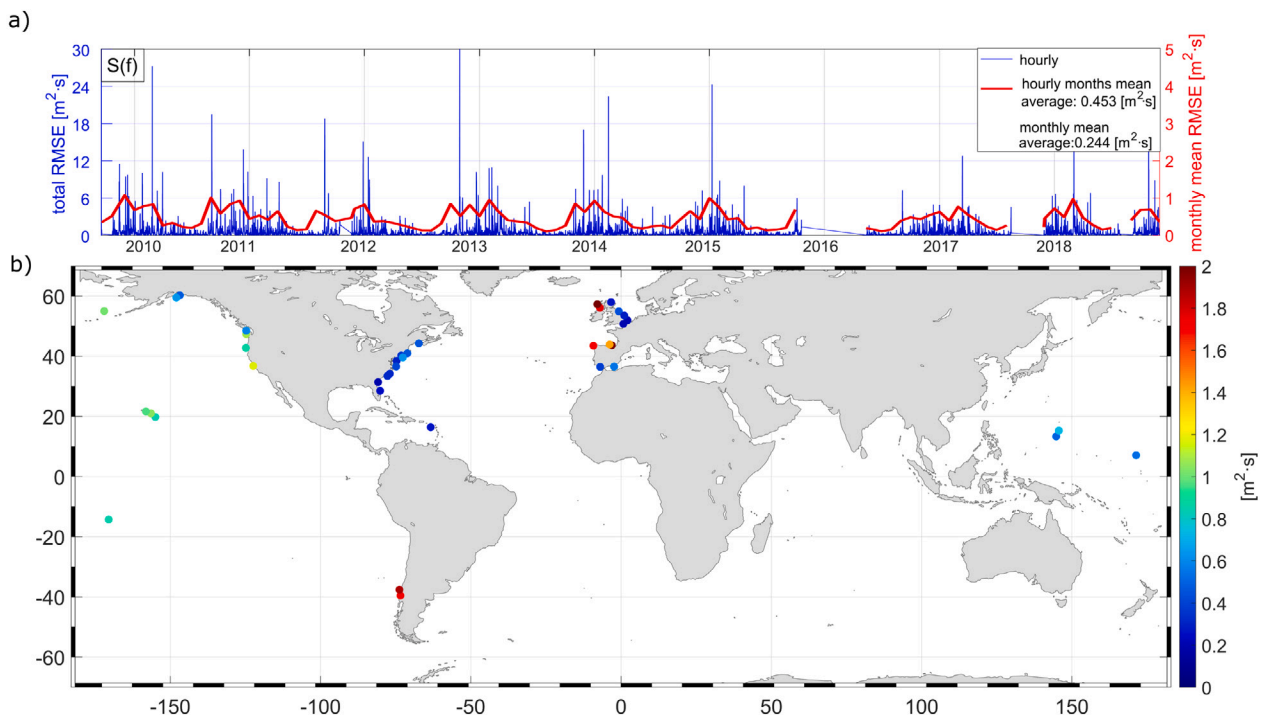


Fig. 5. Panel (a) illustrates the values of the RMSE metric for hourly data (blue line), hourly monthly average (red line) computed with the *1D Spectrum approach* for the $S(f)$ for the location of CDIP 154. Panel (b) depicts the total average of the RMSE for all the locations concerning the $S(f)$.

low, with maximum in Gata, Bilbao and CEFAS 62046. The Pearson coefficient stays above 0.5 for almost every location, the minimum value is found again in Gata and CDIP 163. The SI metric is low, between 0.4–0.7, with the worst values in NOAA 41009, CEFAS 6201058 and CDIP 163. *IDS* for $S(f)$ shows, overall, a SI that ranges between 0.4–1,

the worst results are in Gata with 1.045, CDIP 121, CEFAS 6201058 and NOAA 41009. In contrast, the Ccoef is high, it stays over 0.7 for almost every location. [Table 2](#), overall, shows a good agreement between the directional wave spectrum of the hindcast and the buoy. These results lead to the main analysis of this study, the suitability of the JONSWAP

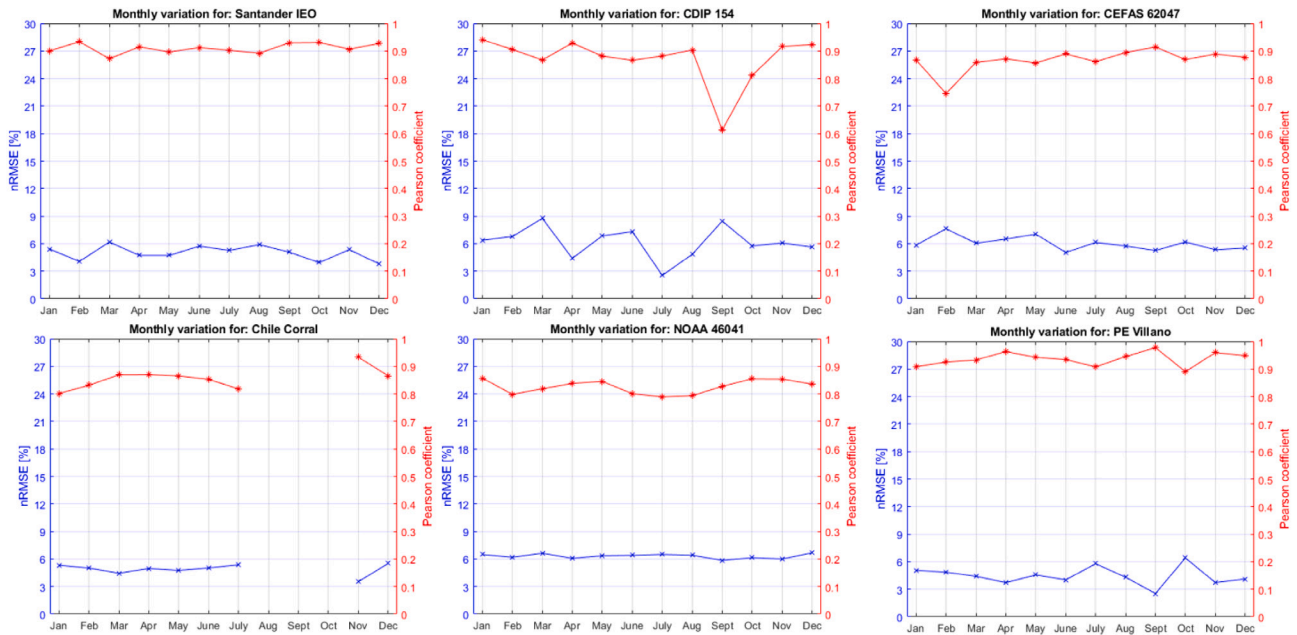


Fig. 6. Matrix approach, red asterisked line is the matrix Pearson coefficient for the monthly mean $S(f, \theta)$, blue x crossed line represents the matrix nRMSE for the monthly mean $S(f, \theta)$.

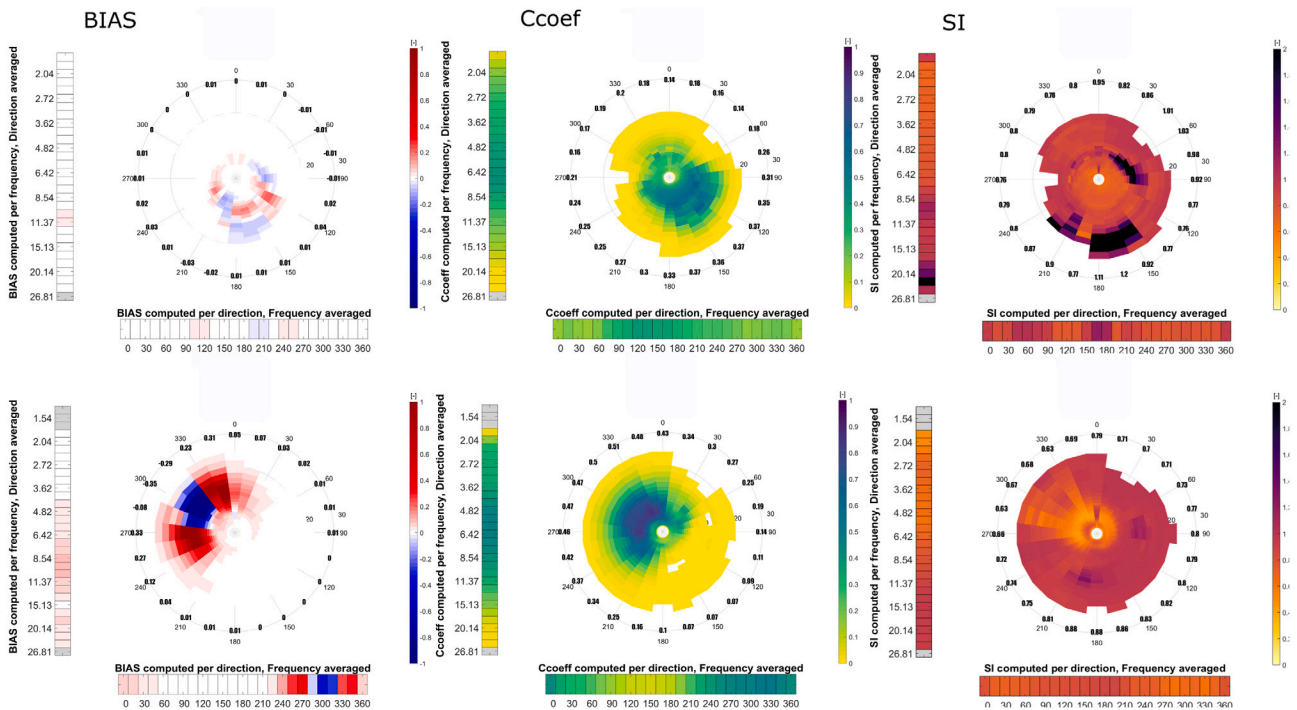


Fig. 7. Polar approach (BIAS, Pearson and SI) computed for the locations of CDIP 154 (upper panel) and Santander (IEO) (lower panel). The bar graphs illustrated below the polar graph and on its left represent the values of the polar graph averaged on the frequencies and direction respectively, the bar on the right is the colorbar.

spectrum worldwide over 30 years (3-hourly data) in nearshore and offshore locations. The best fit of the JONSWAP spectrum is computed finding the value of the γ which minimizes the SI between the hindcast and the JONSWAP spectrum.

5.2. Analysis of the JONSWAP suitability

After the validation of the directional wave spectrum, of the GOW2 the hindcast, the suitability of JONSWAP spectrum is analysed at global scale.

Fig. 8, panel (a), shows the 30-years averaged γ_{best} . In general, the estimated γ varies from 1 to 2. The highest values of the peak-enhancement factor are found along with Central America (Pacific Coast $\gamma \sim 2$), in Hudson Bay, Bering Sea, Baltic sea, on the East Coast of the Cantabrian Sea, Central East Africa at the latitude of Angola, Mozambique Channel, Bengala Gulf, Indonesia, Ojotks Sea and in the Gulf of Carpentaria. In the rest of the world the γ_{best} is low, close to 1. Standard deviation of the γ_{best} is illustrated in Fig. 8 panel (b). The higher γ_{best} the higher the standard deviation. In these regions, the standard deviation is higher than 1 [m²/Hz], while in the rest of

Table 2

GA_b: global approach (b), comparison of the time-averaged directional wave spectra, *MA*: matrix approach, comparison of the directional wave spectrum through the frequency-direction bins, the time-averaged values are shown and *IDS*: 1D spectrum approach for the $S(f)$, the values shown are time-averaged. The illustrated metrics are: nRMSE: Normalized Root Mean Square Error, SI: Similarity Index and Ccoef: Pearson coefficient.

Approaches Buoys	<i>GA_b</i>		MA			IDS ($S(f)$)	
	Metrics		nRMSE	SI	Ccoef	SI	Ccoef
	nRMSE	SI					
CDIP 106	4.0272	0.38	9.331	1.256	0.472	0.870	0.851
CDIP 121	8.3152	0.61	10.662	1.306	0.533	0.933	0.844
CDIP 154	5.9304	0.36	11.673	1.018	0.536	0.683	0.809
CDIP 163	10.852	1.1	11.102	1.544	0.273	0.866	0.844
CDIP 187	7.4832	0.42	10.584	0.841	0.632	0.486	0.882
CDIP 188	9.5221	0.42	10.635	0.813	0.655	0.457	0.893
CDIP 189	9.126	0.65	8.376	1.180	0.459	0.561	0.823
CDIP 197	11.598	0.68	10.508	1.340	0.403	0.805	0.872
CEFAS 6201058	5.7442	0.37	8.842	1.580	0.500	0.989	0.792
CEFAS 62046	11.676	0.56	15.483	0.953	0.461	0.674	0.776
CEFAS 62047	7.1198	0.6	6.344	1.020	0.688	0.522	0.888
CEFAS 62048	5.3909	0.4	6.372	0.923	0.706	0.467	0.910
CEFAS 62288	6.2987	0.39	12.676	1.212	0.504	0.882	0.756
CEFAS 62289	15.055	0.66	8.322	1.322	0.594	0.790	0.822
CEFAS 62293	10.248	0.49	8.496	0.981	0.630	0.610	0.832
Chile Corral	4.7854	0.65	5.718	1.392	0.684	0.748	0.832
Chile Lebu	5.2939	1.04	5.703	1.734	0.642	0.737	0.865
NOAA 41008	8.9685	0.74	8.570	1.765	0.497	0.813	0.779
NOAA 41009	8.4939	0.69	7.620	2.062	0.530	0.910	0.825
NOAA 41013	12.603	0.53	8.428	1.205	0.570	0.616	0.836
NOAA 41036	9.774	0.45	9.359	1.160	0.571	0.599	0.813
NOAA 42060	11.451	0.5	10.767	1.049	0.577	0.580	0.830
NOAA 44009	14.664	0.63	7.909	1.630	0.519	0.793	0.811
NOAA 44014	12.637	0.69	7.982	1.244	0.583	0.662	0.842
NOAA 44025	12.832	0.6	8.519	1.389	0.523	0.723	0.797
NOAA 44027	9.0823	0.45	9.423	1.446	0.534	0.836	0.779
NOAA 44066	11.112	0.53	8.797	1.323	0.586	0.706	0.813
NOAA 46015	11.379	0.62	7.696	1.447	0.573	0.664	0.804
NOAA 46041	7.2877	0.64	6.423	1.369	0.641	0.581	0.865
NOAA 46042	7.8314	0.76	6.179	1.468	0.595	0.567	0.859
NOAA 46061	13.222	0.78	7.722	1.768	0.513	0.869	0.797
NOAA 46073	11.272	0.45	8.028	1.208	0.618	0.586	0.850
NOAA 46076	11.879	0.63	7.938	1.461	0.523	0.629	0.830
NOAA 46087	8.8711	0.64	9.043	1.321	0.527	0.755	0.779
PE Bilbao	42.839	0.9	14.071	1.078	0.350	0.892	0.518
PE Cadiz	5.3204	0.51	13.042	1.159	0.451	0.835	0.662
PE Gata	27.5	0.81	15.899	1.189	0.242	1.045	0.403
PE Villano	4.488	0.31	8.323	0.981	0.626	0.628	0.832
Santander IEO	4.6468	0.43	5.360	1.284	0.716	0.652	0.876

the world it is lower, around $0.1\text{--}0.3[(\text{m}^2/\text{Hz})^2]$. The skewness of the gamma best is also analysed through the estimation of the asymmetry coefficients Bowley–Yule index (Galbraith and van Norden, 2018) and Fischer skewness index (Doane and Seward, 2011). Both indices show a clear right-skewed distribution.

The resulting value of the γ parameter under storm conditions is also an engineering required parameter. Thus, the γ_{best} associated with the wave flux above quantile 0.999 is studied (Fig. 9 panel (a)). These values are higher than the total average of γ_{best} overall for the West part of the continents, Caribbean Sea, East Coast of Madagascar, East Coast of Australia, East Coast of India and overall the Pacific Islands. In contrast for enclosed seas such as Persian Gulf, Red Sea, Mexican Gulf, Northern Sea, Yellow Sea, Andaman Sea, Gulf of Carpentaria and Australia (except the East Coast). In these regions the storms are not associated with a high γ , but with a lower γ , meaning a broader frequency spectrum. These regions are also the ones which have lower standard deviation. Panel (b) illustrates the averaged 10 maxima γ_{best} . Only East part of the continents seems to not reach the top values close to seven, showing values of γ_{best} around 4. This behaviour can be explained because the western part of the continents have a rougher wave climate than the eastern part, as a result of longer generation fetches (Young, 1999).

In order to show regional climate issues, two regions are illustrated in Fig. 10. The first one is the North-East Atlantic Ocean (Fig. 10

panel (a)) including also two enclosed Seas, the Mediterranean Sea and the Baltic Sea. This region is selected because the γ_{best} and its standard deviation is low, whereas the averaged 10 maxima are high (approximately 7). The latter is in the South-West Pacific Ocean (Fig. 10 panel (b)) covering the Australian Coast and New Zealand. Concerning the 10 maxima over 30-years, the Australian continent shows on the East coast lower values of γ_{best} than on the West coast. However, larger SI values indicate bad performance of the JONSWAP (e.g. multi-peaked or broad spectra). In Fig. 10 panel (a), the average γ_{best} is around 1–1.8 in the majority of the locations, while the values are higher in some areas of the Baltic Sea and the Adriatic Sea. The value of the SI is for most of the locations between 0.2 and 0.4, except for UK the coast that goes from the Celtic Sea to Denmark and Southern Norway as for Morocco and Canary Islands, where the value of SI is over 0.4. Fig. 10 panel (b) shows low γ_{best} for the East Coast, including the coast of New Zealand. In this area, the SI is high, meaning that the JONSWAP represents badly the real sea state condition. In contrast, the West coast shows higher values, going from 1.6 to 1.8, and lower the value of SI, which ranges 0.2–0.4 in the Southern area. The highest values of γ_{best} are reached in the Gulf of Carpentaria and on the West coast of Indonesia. The Gulf of Carpentaria shows values of γ_{best} ranging from 2 to 3, while in the West coast of Indonesia from 2 to 2.4. For the former the values of SI are low, whereas for the latter, the values of SI are included between 0.4 and 0.2.

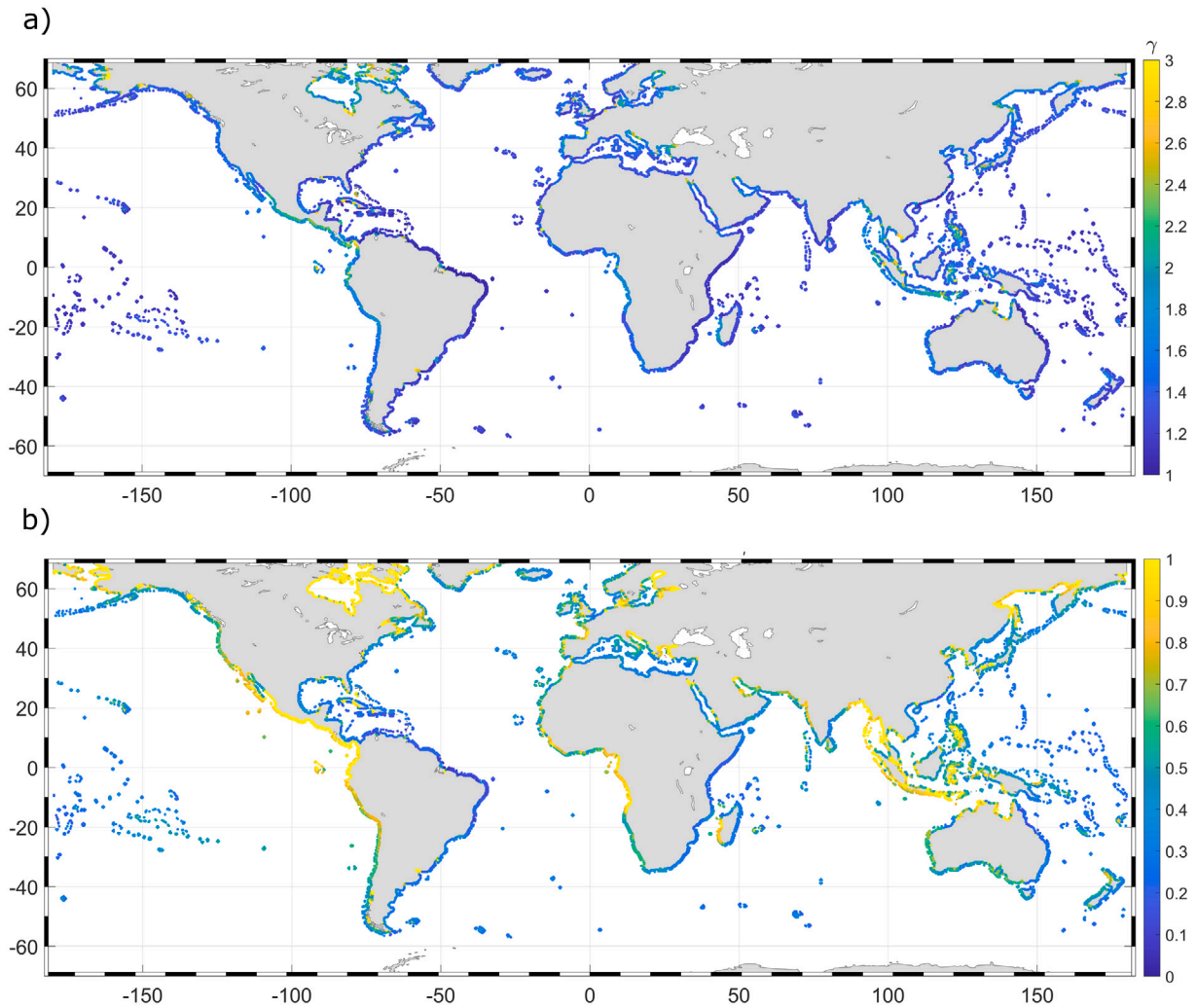


Fig. 8. Average γ_{best} (panel (a)) and total standard deviation of the γ_{best} (panel (b)).

So far we have shown the performance of the JONSWAP considering the climatic conditions during the whole 30-year period. In addition to this analysis, it is important to have a climate point of view showing the yearly variation of the γ_{best} from 1989 to 2018. Larger variations between years are found in the West coast of Central America, Adriatic Sea, Baltic Sea and in the Gulf of Carpentaria (Fig. 8, panel (b)). In these areas the γ_{best} oscillates from 2 to 3. In the rest of the regions, the γ_{best} has lower fluctuation. Although the yearly mean γ_{best} has low fluctuation in some specific areas, the yearly maximum value of γ_{best} presents higher fluctuations (not shown). The areas in which the difference in the maximum γ_{best} is higher, are found in the West Coast of South America at the latitude of Peru and Chile, the West Coast of Australia (region of Western Australia), the Northern shore of Norway, the coast of Portugal, Northern Spain, India, Western Africa, East Coast of North America and the West Coast of New Zealand. For example, in 1989 the maximum value of γ_{best} is around 7 in Western South America, while in 1990 the maximum is around 5. In general, there is a downturn in 1990, while in 1991 the values grow again. Also the standard deviation of the γ_{best} oscillates during the years in the same regions mentioned before. Europe from 1993 to 1998 has the smallest values of SI, whereas the West coast of India has a fluctuating trend. SI remains stable with small fluctuations during the years for the majority of the areas of the world. The highest values of the SI (meaning bad representation of the real sea state) are on the North-West Australian Coast and around the whole coast of India (Fig. 11). India has also the highest oscillation of this parameter. The biggest difference between

the year 1989 and 2018 concerning the mean value of γ_{best} are found in the West Coast of Central America. In 1989 the average value goes from 2.2 to 3, whereas in 2018 it ranges only 2.2 to 2.5. In contrast, the standard deviation does not show relevant interannual variability (not shown). We also study the monthly and seasonal variation of the γ_{best} (not shown). The highest monthly changes are situated in Central East Pacific Ocean (2.6 (April) to 1.6 (September)), Northern Baltic Sea (2.8 (April) to 1.2 (Dec)), Sea of Okhotsk (2.8 (Mar) to 1.2 (Dec)), Bay of Bengal (2.8 (February) to 1 (July)), Central West Indian Ocean (2.8 (April) to 1.5 (December)) and in the Bering Sea (2.4 (March) to 1 (August)). Concerning the seasonal variation, the higher the standard deviation the higher the seasonal variation. Seasons are considered as: DJF (December, January and February), MAM (March, April and May), JJA (June, July and August) and SON (September, October and November). Southern Hemisphere shows similar values through seasons, whereas in the Northern Hemisphere the most different seasons are MAM and SON.

Fig. 11 illustrates the percentage of the time in which the SI is ≤ 0.4 . The SI for the γ_{best} stays over 60% in the Southern area of South America, South Africa, Northern East Madagascar, Southern Australia and New Zealand, the Gulf of Carpentaria, the East Coast of the Asian continent, Indonesia, Bering Sea, Gulf Of Alaska, East Coast of the Central and North America, Baltic Sea, Mediterranean Sea, Red Sea and the Persian Gulf. The highest percentage of time (over 80%) where SI ≤ 0.4 , is in the Japan Sea, the Persian Gulf, Mediterranean Sea, Baltic Sea and the Caribbean Sea. It means that in these regions the use of

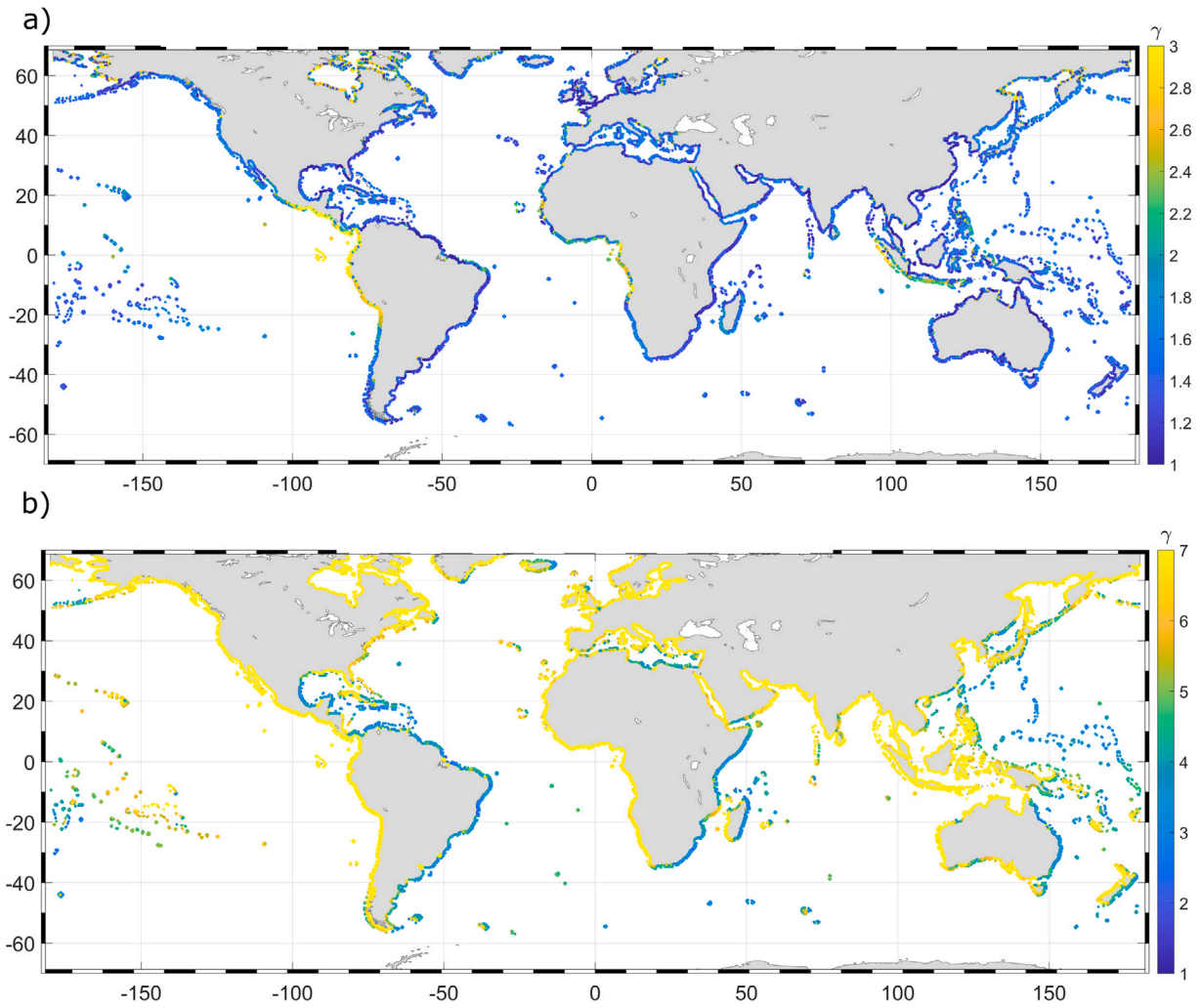


Fig. 9. Total averaged γ_{best} associated with a wave flux over quantile 0.999 (a). The averaged 10 maximum γ_{best} during the 30 historical years analysed.

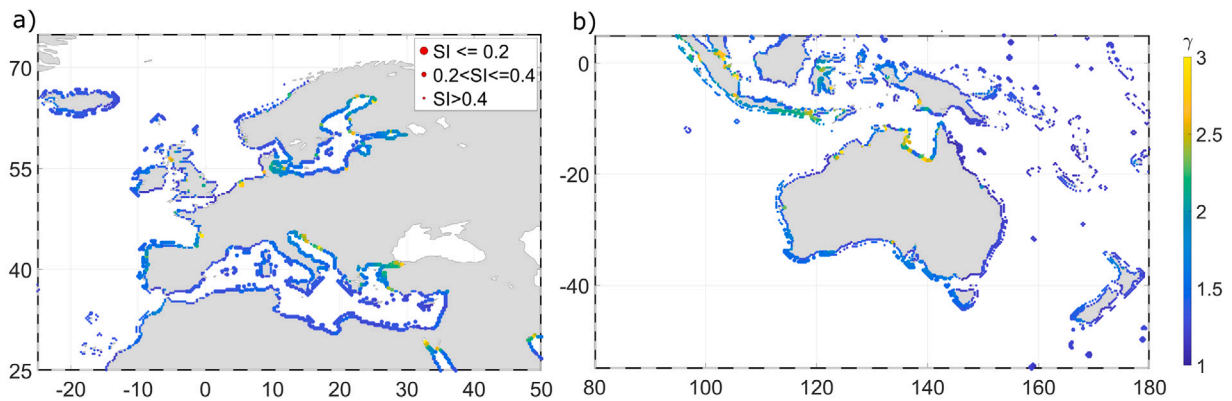


Fig. 10. Total mean γ_{best} (coloured dots) and Scatter Index (size of the dots). Small dots: $SI > 0.4$, medium dots $0.2 \leq SI \leq 0.4$ and big dots $SI \leq 0.2$.

the JONSWAP spectrum is appropriated. The regions in which the SI is higher than 0.4, the JONSWAP spectrum is not recommended. Fig. 11 depicts the 30-years averaged SI. Enclosed and semi enclosed seas have a lower SI, meaning good suitability of the JONSWAP spectrum.

6. Conclusions

The results presented here show a detailed analysis of a comprehensive JONSWAP climate assessment and best fitting on the coastal

region worldwide. We apply a method to compute γ_{best} minimizing the SI between the JONSWAP and the hindcast frequency spectrum. To perform the study of the JONSWAP climate assessment, it is necessary to have a reliable global hindcast directional wave spectrum. Four approaches are proposed to validate the directional wave spectrum following climate and engineering points of view: the global, the matrix, the polar and the 1D spectrum approach. The comparison is carried out with 39 buoys worldwide, overall the hindcast directional wave spectrum shows a good agreement with the buoy data. Concerning the

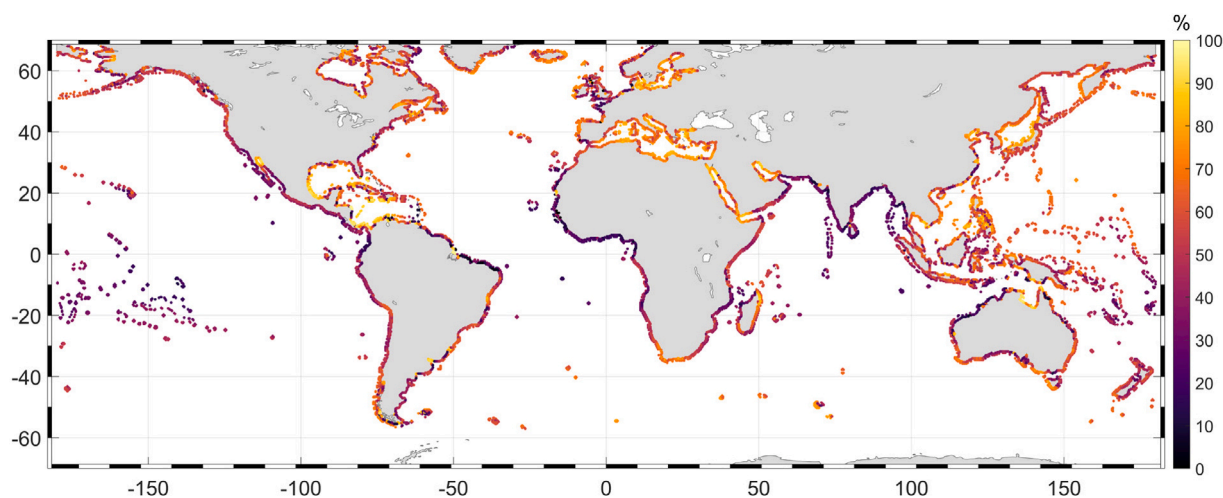


Fig. 11. Percentage of the time in which the SI metric is ≤ 0.4 .

matrix approach (for monthly comparison) the Pearson coefficient is very high, above 0.8 and the nRMSE is below 9%. The polar approach indicates low errors in the hindcast and the same directional dispersion as the buoy. The Pearson and the SI metric coefficients show that the higher the energy the higher the agreement. An extension of this study in areas with waves induced by tropical cyclones and in highest latitudes where the ice coverage information is relevant would be desirable.

The JONSWAP climate analysis, overall, shows that the 30-years averaged global γ_{best} is lower than the standard JONSWAP ($\gamma = 3.3$), with a global estimated value of about ~ 1.54 . As the peak-enhancement factor of the JONSWAP spectrum represents the sharpness of the spectral peak, the 30-years averaged conditions are associated with a broader JONSWAP spectrum. γ_{best} associated with the most energetic sea states (above the quantile 0.999 of the wave energy flux) presents values lower than the standard JONSWAP, such as Caribbean, East coast of South America, Southern Mediterranean Sea, East coast Africa, Madagascar and Australia (Fig. 9(b)). In contrast, in the West Coast of Central America, the Coast of Angola, and the northern Baltic Sea the value of γ_{best} associated with the most energetic events presents values around $3 \sim 3.4$. In these regions, the energetic events show the need to be represented with sharp spectra. The value of γ significantly increases for the averaged 10 maximum γ_{best} during the 30 historical years analysed. The value of γ_{best} are around the top value (i.e. 7) along the West coast of the continents (in these regions the stormy wave conditions are associated with very sharp spectra), whereas the East part of the continents shows lower values, closer to $2 \sim 3.3$. Variations within the months and seasons are found not very significant, whereas interannual variations are stronger in Pacific Coast of Central America.

The global study shows that the JONSWAP spectrum is suitable in some regions of the world. SI under 0.4 for more than 60% of the time seems to be a good indicator of the suitability of JONSWAP. For the locations where the above condition is met the JONSWAP spectrum, with the best estimated local γ , can be used. The γ estimates depend on the studied sea state conditions. Average sea state conditions have lower values of γ , whereas conditions associated to the highest sea conditions (e.g annual maxima) show higher values. There are some locations in which the fitness of the JONSWAP spectrum is not recommended due to multiple factors, such as the presence of high energetic swells and the concurrence of different wave systems (e.g. wind sea and multiple swells). According to these criteria, in regions as the West Coast of Central America, the North-East coast of Brazil, the Gulf of Guinea, India and the North of Western Australia, the JONSWAP spectrum is not recommended (Fig. 11). Understanding the wave systems is still an open issue and, multiple studies are carried out partitioning the

directional wave spectrum. Once the wind sea, primary and secondary swells are identified, then the wave systems can be processed, combined and analysed (e.g. Portilla-Yandún (2018), Portilla-Yandún et al. (2015), Hanson et al. (2009), Portilla-Yandún et al. (2009)). Further global studies to characterize coexisting climate wave systems would provide useful information. The use of partitioned spectral data can help to improve the fitting of multi peaked theoretical frequency spectra. One of the oldest double peaked theoretical frequency spectrum is the one of Ochi and Hubble (1977), successively Torsethaugen and Haver (2004) proposed another double peaked theoretical frequency spectrum. This is a current and still an open research topic, new studies such as Akbari et al. (2020), proposes a Gaussian model to fit the primary system and a JONSWAP spectrum to fit the secondary systems.

We found that the JONSWAP spectrum is suitable in the Mediterranean Sea, Baltic Sea, Red Sea, Persian Gulf, Caribbean Sea, Gulf of Carpentaria, the West Pacific Ocean (except for some coastal regions in Australia and New Zealand) South Africa, and East coast of Madagascar. In these areas, the SI is lower than 0.4 for more than 70% of the historical period. In other regions, such as Northern Brazil, the coast from Mauritania to Nigeria, India, Central America, Northern West Australia, Northern Sea, East coast of Africa, and West coast of Madagascar, the JONSWAP spectrum performs badly, with SI lower than 0.4 only for the 35% of the time or lower.

Two specific coastal regions are studied, Oceania and Europe. Regarding Europe, overall in the Mediterranean Sea, Portugal, and Northern Spain, Baltic Sea, Island and West Ireland the JONSWAP spectrum seems to perform well. Concerning Oceania, the performance of the JONSWAP spectrum is worse than in Europe. To conclude, the performance of the JONSWAP spectrum varies for each region of the world, and a fitting of the real wave conditions for a specific location is desirable. Overall, the JONSWAP spectrum with the best γ is suitable (where the $SI \leq 0.4$ for more than 60% of the total time) for the 37.7% of the coasts worldwide.

Declaration of competing interest

The authors declare that they have no known competing financial interests or personal relationships that could have appeared to influence the work reported in this paper.

Data availability

Data will be made available on request.

Acknowledgements

This work is funded by the Spanish State Research Agency through the project EXCEED (RTI2018-096449-B-I00). H.L. acknowledges the financial support from the Spanish Ministry of Universities (Grant 578 FPU17/06203). We thank the reviewers for their valuable comments and suggestions.

References

- Akbari, H., Panahi, R., Amani, L., 2020. Improvement of double-peaked spectra: revisiting the combination of the Gaussian and the JONSWAP models. *Ocean Eng.* 198, 106965.
- Amante, C., Eakins, B.W., 2009. ETOPO1 arc-minute global relief model: procedures, data sources and analysis.
- Amuro, S., Ewans, K., 2019. The effect of swell on wave spectra of extreme sea states offshore Sarawak, Malaysia. *Ocean Eng.* 189, 106288.
- Ardhuin, F., O'Reilly, W., Herbers, T., Jessen, P., 2003. Swell transformation across the continental shelf. Part I: Attenuation and directional broadening. *J. Phys. Oceanogr.* 33 (9), 1921–1939.
- Ardhuin, F., Rogers, E., Babanin, A.V., Filipot, J., Magne, R., Roland, A., van der Westhuysen, A., Queffelec, P., Lefevre, J., Aouf, L., Collard, F., 2010. Semiempirical dissipation source functions for ocean waves. Part I: definition, calibration, and validation. *J. Phys. Oceanogr.* 40 (9), 1917–1941.
- Atkinson, L., Bushnell, M., Franke, G., 2005. Second workshop report on the quality assurance of real-time ocean data: Waves and currents (QARTOD-II). Norfolk, VA USA.
- Barstow, S.F., Bidlot, J.-R., Caires, S., Donelan, M.A., Drennan, W.M., Dupuis, H., Graber, H.C., Green, J.J., Gronlie, O., Guérin, C., et al., 2005. Measuring and analysing the directional spectrum of ocean waves.
- Battjes, J.A., Janssen, J., 1978. Energy loss and set-up due to breaking of random waves. *Coast. Eng. Proc.* (16), 32.
- Benoit, M., 1993. Practical comparative performance survey of methods used for estimating directional wave spectra from heave-pitch-roll data. *Coast. Engineering* 62–75.
- Brown, R., Baker, J., McCall, J., 2001. Characteristics for extreme sea states on the Norwegian continental shelf. Technical report, NBDC, NOAA, National Oceanic and Atmosphere Administration. Marshall D.Earle, Neptune Science, Inc. 150 Cleveland Avenue, Slidell, Louisiana 70458.
- Camus, P., Mendez, F.J., Medina, R., 2011. A hybrid efficient method to downscale wave climate to coastal areas. *Coast. Eng.* 58 (9), 851–862.
- Corbella, S., Pringle, J., Stretch, D.D., 2015. Assimilation of ocean wave spectra and atmospheric circulation patterns to improve wave modelling. *Coast. Eng.* 100, 1–10.
- Craciunescu, C.C., Christou, M., 2020. Wave breaking energy dissipation in long-crested focused wave groups based on JONSWAP spectra. *Appl. Ocean Res.* 99, 102144.
- Doane, D.P., Seward, L.E., 2011. Measuring skewness: A forgotten statistic? *J. Stat. Educ.* 19 (2).
- Earle, M., Steele, K., Wang, D., 1999. Use of advanced directional wave spectra analysis methods. *Ocean Eng.* 26 (12), 1421–1434.
- Echevarria, E., Hemer, M., Holbrook, N., 2019. Seasonal variability of the global spectral wind wave climate. *J. Geophys. Res. Oceans* 124 (4), 2924–2939.
- Friesch, J., Kim, K.-H., Andersen, P., Bark, G., Chang, B., Di Felice, F., Sasaki, N., 2002. The specialist committee on cavitation induced pressures, final report and recommendations to the 23rd ITTC. In: 23rd International Towing Tank Conference. INSEAN The Italian Ship Model Basin.
- Galbraith, J., van Norden, S., 2018. Business cycle asymmetry and unemployment rate forecasts. In: Working paper. Technical report.
- García-Gabín, W., 2015. Wave bimodal spectrum based on swell and wind-sea components. *IFAC-PapersOnLine* 48 (16), 223–228.
- Goda, Y., 1988. *Random Seas and Design of Maritime Structures*. World Scientific.
- Hanson, J.L., Tracy, B.A., Tolman, H.L., Scott, R.D., 2009. Pacific hindcast performance of three numerical wave models. *J. Atmos. Ocean. Technol.* 26 (8), 1614–1633.
- Hashimoto, N., Konbune, K., 1988. Directional spectrum estimation from a Bayesian approach. *Coast. Eng. Proc.* (21), 4.
- Hasselmann, K., Barnett, T., Bouws, E., Carlson, H., Cartwright, D., Enke, K., Ewing, J., Gienapp, H., Hasselmann, D., Kruseman, P., et al., 1973. Measurements of wind-wave growth and swell decay during the joint north sea wave project (JONSWAP). *Ergänzungsheft* 8–12.
- Hasselmann, D.E., Dunckel, M., Ewing, J., 1980. Directional wave spectra observed during JONSWAP 1973. *J. Phys. Oceanogr.* 10 (8), 1264–1280.
- Hasselmann, S., Hasselmann, K., Allender, J., Barnett, T., 1985. Computations and parameterizations of the nonlinear energy transfer in a gravity-wave spectrum. Part II: Parameterizations of the nonlinear energy transfer for application in wave models. *J. Phys. Oceanogr.* 15 (11), 1378–1391.
- Holthuijsen, L., 2007. *Waves in Oceanic and Coastal Waters*. Cambridge University Press.
- Iriah, J.L., Wozencraft, J.M., Cunningham, A.G., 2000. Lidar sensor for measuring directional-spectral characteristics of water waves. Technical report, Corp of engineers mobile al joint airborne lidar bathymetry technical center of expertise.
- Kamphuis, J.W., 2010. *Introduction To Coastal Engineering and Management*. vol. 30, World Scientific.
- Kuik, A., Van Vledder, G.P., Holthuijsen, L., 1988. A method for the routine analysis of pitch-and-roll buoy wave data. *J. Phys. Oceanogr.* 18 (7), 1020–1034.
- Leonard, B.P., 1979. A stable and accurate convective modelling procedure based on quadratic upstream interpolation. *Comput. Methods Appl. Mech. Engrg.* 19 (1), 59–98.
- Leonard, B.P., 1991. The ULTIMATE conservative difference scheme applied to unsteady one-dimensional advection. *Comput. Methods Appl. Mech. Engrg.* 88 (1), 17–74.
- Longuet-Higgins, M.S., 1961. Observations of the directional spectrum of sea waves using the motions of a floating buoy. *Ocean Wave Spectr.*
- Lu, G.Y., Wong, D.W., 2008. An adaptive inverse-distance weighting spatial interpolation technique. *Comput. Geosci.* 34 (9), 1044–1055.
- Lygre, A., Krogstad, H.E., 1986. Maximum entropy estimation of the directional distribution in ocean wave spectra. *J. Phys. Oceanogr.* 16 (12), 2052–2060.
- Magnusson, A.K., Vårdal, O.T., Hjøllø, B.Å., MyMebust, R., Reistad, M., Hansen, K., 2001. Forecasting wave-induced response for offshore floating structures. In: The Eleventh International Offshore and Polar Engineering Conference. OnePetro.
- Mazaheri, S., Imani, H., 2019. Evaluation and modification of JONSWAP spectral parameters in the Persian Gulf considering offshore wave characteristics under storm conditions. *Ocean Dyn.* 1–25.
- Mitsuyasu, H., Tasai, F., Suhara, T., Mizuno, S., Ohkusu, M., Honda, T., Rikiishi, K., 1980. Observation of the power spectrum of ocean waves using a cloverleaf buoy. *J. Phys. Oceanogr.* 10 (2), 286–296.
- Ochi, M.K., Hubble, E.N., 1977. Six-parameter wave spectra. In: *Coastal Engineering*. pp. 301–328.
- Onorato, M., Osborne, A.R., Serio, M., Bertone, S., 2001. Freak waves in random oceanic sea states. *Phys. Rev. Lett.* 86 (25), 5831.
- O'Reilly, W., Herbers, T., Seymour, R., Guza, R., 1996. A comparison of directional buoy and fixed platform measurements of Pacific swell. *J. Atmos. Ocean. Technol.* 13 (1), 231–238.
- Perez, J., Menendez, M., Losada, I.J., 2017. GOW2: A global wave hindcast for coastal applications. *Coast. Eng.* 124, 1–11.
- Phillips, O.M., 1958. The equilibrium range in the spectrum of wind-generated waves. *J. Fluid Mech.* 4 (4), 426–434.
- Pierson, W.J., 1976. The theory and applications of ocean wave measuring systems at and below the sea surface, on the land, from aircraft, and from spacecraft.
- Portilla-Yandún, J., 2018. The global signature of ocean wave spectra. *Geophys. Res. Lett.* 45 (1), 267–276.
- Portilla-Yandún, J., Cavaleri, L., Van Vledder, G.P., 2015. Wave spectra partitioning and long term statistical distribution. *Ocean Model.* 96, 148–160.
- Portilla-Yandún, J., Ocampo-Torres, F.J., Monbaliu, J., 2009. Spectral partitioning and identification of wind sea and swell. *J. Atmos. Ocean. Technol.* 26 (1), 107–122.
- Rossi, G.B., Crenna, F., Piscopo, V., Scamardella, A., 2020. Comparison of spectrum estimation methods for the accurate evaluation of sea state parameters. *Sensors* 20 (5), 1416.
- Rueda-Bayona, J.G., Guzmán, A., Silva, R., 2020. Genetic algorithms to determine JONSWAP spectra parameters. *Ocean Dyn.* 70 (4), 561–571.
- Saha, S., Moorthi, S., Pan, H.-L., Wu, X., Wang, J., Nadiga, S., Tripp, P., Kistler, R., Woollen, J., Behringer, D., Liu, H., Stokes, D., Grumbine, R., Gayno, G., Wang, J., Hou, Y.-T., Chuang, H.-Y., Juang, H.-M.H., Sela, J., Iredell, M., Treadon, R., Kleist, D., Van Delst, P., Keyser, D., Derber, J., Ek, M., Meng, J., Wei, H., Yang, R., Lord, S., Van Den Dool, H., Kumar, A., Wang, W., Long, C., Chelliah, M., Xue, Y., Huang, B., Schemm, J.-K., Ebisuzaki, W., Lin, R., Xie, P., Chen, M., Zhou, S., Higgins, W., Zou, C.-Z., Liu, Q., Chen, Y., Han, Y., Cucurull, L., Reynolds, R.W., Rutledge, G., Goldberg, M., 2010. The NCEP climate forecast system reanalysis. *Bull. Am. Meteorol. Soc.* 91 (8), 1015–1057.
- Saha, S., Moorthi, S., Wu, X., Wang, J., Nadiga, S., Tripp, P., Behringer, D., Hou, Y.-T., Chuang, H.-y., Iredell, M., et al., 2014. The NCEP climate forecast system version 2. *J. Clim.* 27 (6), 2185–2208.
- Steele, K., Lau, J., Hsu, Y.-H., 1985. Theory and application of calibration techniques for an NDBC directional wave measurements buoy. *IEEE J. Ocean. Eng.* 10 (4), 382–396.
- Takezawa, S., Kobayashi, K., 1989. On the motion responses of offshore floating structures in directional spectra waves the 1st-order responses. *J. Society of Naval Archit. Japan* 1989 (165), 141–152.
- The WAVEWATCH III® Development Group, 2016. User manual and system documentation of WAVEWATCH III® version 5.16. Tech. Note, (329), NOAA/NWS/NCEP/MMAB, College Park, MD, USA, 326 pp. + Appendices.
- Tolman, H.L., 2002. Alleviating the garden sprinkler effect in wind wave models. *Ocean Model.* 4 (3–4), 269–289.
- Tolman, H.L., 2003. Treatment of unresolved islands and ice in wind wave models. *Ocean Model.* 5 (3), 219–231.

- Tolman, H.L., 2014. The WAVEWATCH III Development Group: User manual and system documentation of WAVEWATCH III version 4.18. Technical Note, Environmental Modeling Center, National Centers for Environmental Prediction, National Weather Service, National Oceanic and Atmospheric Administration, US Department of Commerce, College Park, MD.
- Tomas, A., Mendez, F.J., Losada, I.J., 2008. A method for spatial calibration of wave hindcast data bases. *Cont. Shelf Res.* 28 (3), 391–398.
- Torsethaugen, K., 1993. A two peak wave spectrum model.
- Torsethaugen, K., Haver, S., 2004. Simplified double peak spectral model for ocean waves. In: *The Fourteenth International Offshore and Polar Engineering Conference*. OnePetro.
- WAFO Group, 2011. A matlab toolbox for analysis of random waves and loads.
- Wang, Y., 2014. Calculating crest statistics of shallow water nonlinear waves based on standard spectra and measured data at the Poseidon platform. *Ocean Eng.* 87, 16–24.
- Young, I., 1999. Seasonal variability of the global ocean wind and wave climate. *Int. J. Climatol.: A J. Roy. Meteorol Soc.* 19 (9), 931–950.